Available online at www.sciencedirect.com

ScienceDirect

Energy Procedia 69 (2015) 279 – 288

Energy Procedia

International Conference on Concentrating Solar Power and Chemical Energy Systems, SolarPACES 2014

Geometrical shape optimization of a cavity receiver using coupled radiative and hydrodynamic modeling

C.-A. Asselineau[a],*, J. Zapata[a], and J. Pye[a]

[a]*The Australian National University, Research School of Engineering, Canberra, ACT 0200, Australia.*

Abstract

By using a two-stage optimisation process we maximise the heat rate output of a four-parameter axisymmetric direct steam generation cavity receiver. The model includes radiative and hydrodynamic considerations. We show that a significant range of geometrical shapes show similar efficiencies while having different wall flux and temperature profiles.

Peer review by the scientific conference committee of SolarPACES 2014 under responsibility of PSE AG

Keywords: Receiver, Ray-tracing, Hydrodynamics, Heat-transfer, Optimisation.

1. Introduction

In concentrated solar power systems, receivers convert concentrated solar radiation into heat and consequently have a major impact on overall system efficiency and economic viability. Increasing the temperature of operation of existing receivers offers non negligible thermodynamic efficiency gains, as stated by the Carnot theorem; however, higher receiver temperatures translate into higher energy losses at the receiver location. Among the options envisioned to convert concentrated solar radiation into heat, indirect heating of a heat carrier circulating in irradiated tubes has been favored up to now in commercial applications. At high temperatures, cavity receivers can offer an advantage to contain emissive losses and thus improve the overall efficiency of the system. Recently, several studies

---

* Corresponding author. Tel.: +69-04-9870-1853
E-mail address: charles-alexis.asselineau@anu.edu.au

1876-6102
Peer review by the scientific conference committee of SolarPACES 2014 under responsibility of PSE AG
doi:10.1016/j.egypro.2015.03.032

Nomenclature

r	Radius, m
l	Length, m
$\dot{Q}$	Radiative power, W
J	Radiosity, W
n	Tube element index
g	Total number of geometries for an optimisation
N	Raytrace scale array
	Absorptivity
ε	Emissivity
σ	Standard deviation
F_{ij}	View factor of element i looking at element j
IC_{tot}	Overall amplitude of the confidence interval
p	Population of receiver geometries
γ	Convective heat transfer coefficient, W/m^{2}K
x	Steam quality
T	Temperature, K
P	Pressure, Pa
h	Enthalpy, kJ/kg
ρ	Fluid density, kg/m^3
A	Area, m^2
D	Internal diameter of the tube, m

Subscripts:

s	Optimisation routine step s
a	Aperture
f	Frustum
c	Cone
r	Receiver
sun	Sun
fl	Fluid
w	Wall
abs	Absorbed
emit	Emitted via thermal emissions
abs net	Net absorbed: absorbed - emitted

focused on cavity geometry optimization for different purposes: to average the flux on the internal walls of the receiver [1], to minimize overall radiative losses [2], to improve optical efficiency using bottom convex cylindrical geometry [3] or to study optimal geometrical aspect ratio for cylindrical cavity receivers at the focus of multi-dish concentrators [4]. All these studies agree on the strong influence of cavity shape on flux distribution on the internal walls of the cavity while only taking into account the radiative component of receiver losses. This study proposes an attempt to optimize the shape of a cavity receiver based on its overall thermal efficiency using coupled radiative and hydrodynamic modeling. Convective losses to the environment are not yet considered. The receiver considered is a once through direct steam generation receiver placed at the focus of the SG4 parabolic dish at the Australian National University (ANU) [5]. The geometry of the receiver is defined by a four-parameter axisymmetric profile.

2. Model system

The present study considers a system composed of a parabolic dish concentrator with a cavity receiver placed at its focus. The dimensions of the simulated parabolic dish fit those of the SG4 dish at the ANU [5]. Parasitic absorption of solar radiation due to non ideal reflectivity of the mirrors, and concentrator slope error due to non-ideal orientation of the reflective surface are considered. The SG4 Dish, being in reality an assembly of spherically curved square mirrors and thus has a spatial flux distribution of the reflected radiation that differs from an ideal parabolic concentrator. The Dish model used in this study is a modified parabolic dish implementation able to reproduce experimental measurements of the concentrated flux distribution [5].

The receiver, placed at the focus of the concentrator, is an axisymmetric cavity defined by four geometric parameters: aperture radius r_{a}, cone radius r_{c}, frustum length l_{f} and cone length l_{c}. As shown in Fig. 1, the combination of these four-parameters is able to create a variety of geometries. Cavity walls are considered to be grey and diffuse. Receiver absorptivity α_{r} is set to 0.95 and receiver emissivity ε_{r} is set to 0.85, as if painted with Pyromark® 2500 paint [6]. The receiver is open as opposed to windowed receiver. The internal walls of the receiver are covered by a single coiled tube in which a water/steam mixture circulates. In this study, water enters the receiver at the aperture and leaves it at the tip of the conical section, following the receiver profile. Lastly, the receiver is placed into a cylindrical housing envelope whose radius and length are respectively 100 mm more than the maximum radius and overall length of the receiver geometry (aperture excluded); to account for insulation material space. This limits r_c to a maximum value of 0.65 m.

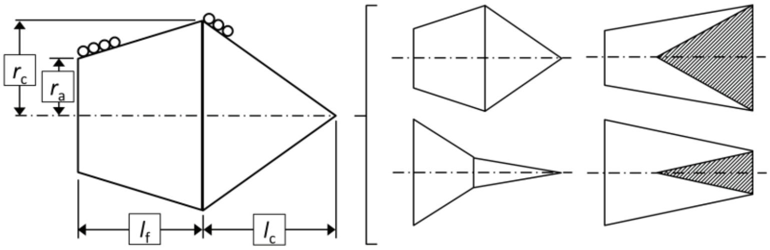

Fig. 1. Four-parameter cavity receiver diagram and examples of geometries.

A Buie sunshape is implemented in order to model the incoming solar radiation [7]. The circum-solar ratio parameter quantifying the amount of radiation coming from outside the solar disc is set to 0.01 [8].

In this study, only heat loss involving radiative heat transfer mode is considered. This heat loss is divided into two categories whether it involves light in the visible or infrared wavelength range in order to differentiate optical processes involved in the concentration process with thermo-radiative emissions. Four types of optical losses involved in the concentration process are distinguished:

- Blockage losses: solar radiation hitting of the receiver housing.
- Dish surface losses: reflectivity of the dish mirrors is set to 0.9.
- Spillage losses: solar radiation missing the receiver after reflection on the dish.
- Reflective losses: solar radiation reflected out of the cavity.

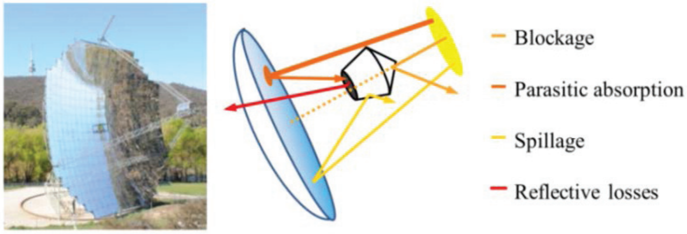

Fig. 2. The Big Dish at the ANU STG facilities (left) and optical losses breakdown diagram (right).

Thermal emissions are computed considering only the receiver internal surface and aperture. Every surface element of the cavity emits radiation according to the Stefan-Boltzmann law [9]. Radiative and hydrodynamic models being coupled in this study, thermal emissions, function of the surface temperature, are indirectly dependent on incoming radiation and hydrodynamic conditions of the flow in the receiver tubes.

3. Four-parameters geometry optimisation method

A two stage optimisation process is used to maximise the net energetic gain of the receiver by studying variations in geometry. The objective of the two-stage division of this process is to separate the computationally intensive geometry exploration phase, where lots of geometries are simulated, from the detailed heat transfer analysis of good geometries.

In the first stage, the preliminary geometry exploration, the receiver geometry is optimised considering only radiative heat transfer with a coarse surface discretisation. $\dot{Q}_{\text{abs net}}$, the amount of radiative power captured subtracted by thermal emission, is maximised. Thermal emissions are here estimated using only two elements per cavity shape and constant temperature estimation for each of these. The second stage is a refined heat transfer simulation that re-evaluates best performing geometries from the first stage by calculating detailed energy balances on the internal walls of the receiver. This advanced heat transfer model uses ray-tracing for radiative heat transfer purposes, a hydrodynamic one-dimensional finite elements tube model to model water/steam flow in the receiver tube, and a refined internal surface discretisation/tube partitioning scheme to couple them.

3.1. First stage: Preliminary geometry exploration

Radiative heat transfer is modeled using Monte-Carlo ray-tracing [9]. As any stochastic integration method, Monte-Carlo ray-tracing shows a variable degree of accuracy depending on the integration parameters. Light is approximated as a bundle or bi-dimensional rays; the more rays cast, the higher the precision. If N is the total number of rays cast, the convergence rate is proportional to $1/\sqrt{N}$ which translates to a doubling of the precision when multiplying by 4 the number of rays cast [10]. For complex scenes, this can lead to very computationally intensive simulations in order to get the desired level of precision.

This study focuses on the optimization of the shape of receivers; numerous geometries have to be evaluated and compared, potentially leading to a very large number of ray-tracing simulations being performed. In this situation, the goal is to maximise the computational value of rays cast by focusing as much as possible on receiver geometries that perform the best, and avoid spending computation time on geometries that have no chance of being optimal. One way to achieve this is to use a sequential optimization process where several geometries are simulated at each step with the number of rays progressively increased from one step to the next. Using statistical estimators of the mean and standard deviation of $\dot{Q}_{\mathrm{abs\,net}}$ at each step, it is possible to measure the performance of each geometry and discard the underperforming ones from progressing further. The law of large numbers predicts a Gaussian distribution on the result of large samples of independent random events, the three sigma rule can be used to estimate the confidence interval of the results at each step of the optimization routine. The $\dot{Q}_{\mathrm{abs\,net}}$ expected value has 99.7% chances to be in an interval of $\pm 3\sigma$ around its mean estimator. At each step s, the overall amplitude of the confidence interval $IC_{\mathrm{tot},s} = 6\sigma_s$ serves as a threshold to discard geometries which performances are almost certainly lower than the best case of the population p_s. Every geometry in p_s which $\dot{Q}_{\mathrm{abs\,net}}$ mean estimator is lower than $max(\dot{Q}_{\mathrm{abs\,net}}) \times (1 - IC_{\mathrm{tot},s})$, quantifying the worst case scenario at the statistical level, is discarded and will not participate to the next iteration.

To explore receiver geometries, this study uses a random search approach. A parameter space is declared at the beginning of the routine and a starting population of geometries is generated by declaring random parameters with uniform probability distribution. The parameter space is a cylinder of specified radius and depth and acts as a bounding box for all random geometries. All variables describing the rest of the scene are kept constant trough the optimisation.

A single confidence interval criterion is used per optimisation step to compare the performances of all competing geometries. This confidence interval evaluated using a different set of test geometries able to cover the parameter space comprehensively and give a good estimation of the ray-trace precision. The generation of 5 test geometries takes place at the beginning of any optimisation run to take into account the specificities of each simulation conditions and follows simple heuristics:

- A: Smallest area configuration
- B: Thin and long concave cone and flat aperture plane.
- C: Average geometry
- D: Cone dominant geometry
- E: Highest area with convex cone

An array describing the number of rays cast per optimisation step, labelled ray-trace scale, is declared and test geometries are simulated. The confidence interval for each step is taken as the highest value of the evaluated $IC_{\mathrm{tot},s} = 6\sigma_s$ for the 5 test-geometries.

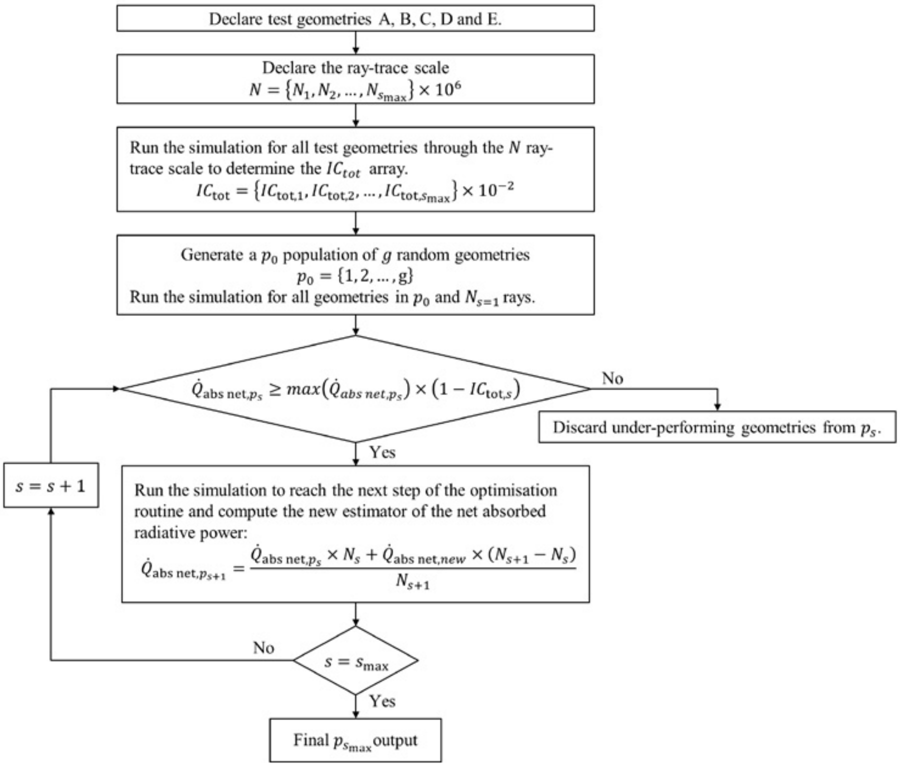

Fig. 3. Radiative heat transfer stochastic optimisation algorithm.

3.2. Second stage: refined heat transfer model

A population $p_{s_{\max}}$ of geometries sharing statistically identical $\dot{Q}_{\mathrm{abs\ net}}$ from a radiative point of view is obtained at the end of the first stage with a first order approximation of the losses. A refined heat transfer model is used to simulate the geometries with more accuracy to differentiate between them. First, a new discretisation scheme that describes different tube sections along the receiver is applied. They are then simulated again using Monte-Carlo ray-tracing with 10,000,000 rays in order to get corresponding absorbed radiative power per tube element $\dot{Q}_{\mathrm{abs}}(n)$. A finite element energy balance of the absorber tube in steady state is used to determine the enthalpy gain of the water/steam mixture as it travels from the inlet of the helical tube, at the aperture, to the outlet situated at the back of the cavity. The temperature of the absorber tube wall is dominated by the evolution of fluid temperature as it goes from saturated liquid to superheated steam.

4. Heat transfer model

This section describes in more details the heat transfer model implementation used in the two-stage optimisation process.

4.1. Optical loss

The specific code used is “Tracer” by Y. Meller, an open-source ray-tracing code written in Python language [11]. The ray-tracing method used by the tracer is sometimes referred to as “path-tracing” where each ray bears a fraction of the energy of the source and absorption/reflection events are directly computed, depleting this energy. Floating point rounding precision issues, potentially corrupting the results of this type of ray-racing, are monitored and handled through by managing rays starting energy and controlling the minimum energy that a ray can bear during the simulation. The random number generator is the native Python implementation using the Mersenne Twister as core generator.

4.2. Thermal emission

Thermal emissions from the internal walls of the receiver to the aperture are calculated using the radiosity problem formulation [9]. View factors matrices required to perform the calculations are obtained through a distinct Tracer-based parametric ray-tracing routine that automatically adapts to any 4 parameters cavity geometry. The precision of the result is controlled through standard deviation estimation of each element of the matrix and standard deviation estimation of the combination rule between all pairs of elements [9]. The flexibility of the method gives the opportunity to perform fast calculations with a lower level of discretization of the receiver surfaces for the optimisation purposes, and more accurate calculations to study finer temperature distributions.

4.3. Hydrodynamics

Pressure and enthalpy are used to specify the state of the fluid through the tube, and are used to calculate other fluid properties (e.g. density, steam quality, viscosity, etc.) and a localized fluid forced convection coefficient $\gamma(n)$. Fluid properties are calculated using freesteam [12] and fluid forced convection coefficients are calculated using single phase correlations [13, 14], or two-phase flow correlations [15, 16], depending on the local steam quality $x(n)$. Using these properties, it is possible to formulate simplified relations for pressure loss and enthalpy gain in each tube segment:

$$P(n+1) = P(n) - \frac{\dot{m}l(n)}{2\rho A^2 D(n)} \quad , \quad h(n+1) = h(n) + \frac{\gamma(n)\pi D(n)l(n) \times \left(T_{\mathrm{w}}(n) - T_{\mathrm{fl}}(n)\right)}{\dot{m}} \tag{1}$$

The amount of heat absorbed by the fluid in each segment $\dot{Q}_{\mathrm{fl}}(n)$ is proportional to the difference between the fluid bulk temperature $T_{\mathrm{fl}}(n)$ and the wall temperature $T_{\mathrm{w}}(n)$. The model iteratively solves the balance for each element, updating $P(n)$ and $h(n)$, and recalculating fluid properties at each step until $P(n)$ and $h(n)$ vary less than 0.05% from the previous iteration.

4.4. Tube discretisation

The heat transfer model assumes a constant tube diameter (ID 20mm, OD 26mm) and generates a helical path for the tube that conforms to the candidate geometry. The model then partitions the tube into lengthways segments or bins, which correspond to approximately one turn along the helical path. The resulting model is a finite element representation of the absorber tube with segments of variable length (see Fig. 4). From a geometric perspective, this segmentation can be envisaged as a set of "concentric rings" arranged along the depth of the cavity, where the wall temperature of each segment is assumed uniform. This partitioning scheme yields between 50 and 70 tube segments, depending on the tube size and candidate geometry dimensions considered in this study. The number of segments provides an adequate resolution to resolve the localized energy balances for each segment, under the assumption of bulk fluid properties and uniform tube wall temperatures (see 4.5).

4.5. Tube element energy balance

The balance on the outer wall of the tube elements is performed by varying the tube wall temperature $T_{\mathrm{w}}(n)$. To have an explicit connection between both balances, the model neglects the temperature gradient between the inside and outside of the tube, which is equivalent to neglecting conductive heat transfer resistance through the tube walls. The tube outer energy balance equation is:

$$\dot{Q}_{\mathrm{abs}}(n) - \dot{Q}_{\mathrm{emit}}(n) - \gamma(n)\pi D(n)l(n) \times \left(T_{\mathrm{w}}(n) - T_{\mathrm{fl}}(n)\right) = 0 \tag{2}$$

Where $\dot{Q}_{\mathrm{abs}}(n)$ is obtained by ray-tracing (see 4.1) and $\dot{Q}_{\mathrm{emit}}(n)$ by solving a radiosity method (see 4.2). The model then adjusts $T_{\mathrm{w}}(n)$ of each element until the balance is satisfied. The change in wall temperature requires a new calculation of the fluid energy balance, thereby adding an outer iteration loop to the simulation. To aid the convergence of this calculation, this study performs an initial guess of wall temperatures by assuming that the gain in fluid enthalpy depends exclusively on the absorbed radiation from the concentrator, and a linear pressure drop:

$$P(n+1) \approx P(n) + \Delta P \quad , \qquad h(n+1) \approx h(n) + \frac{\dot{Q}_{\mathrm{abs}}}{\dot{m}} \tag{3}$$

From this initial enthalpy profile, a fluid temperature profile is calculated, and wall temperatures are assumed to be 5°C higher than fluid temperatures, i.e. $T_{\mathrm{w}}(n) \approx T_{\mathrm{fl}}(n) + 5$. The convergence of this loop is monitored by observing that the variation of all wall temperature elements is less than 0.05% of their previous iteration values.

A third and overarching iteration loop adjusts the mass flow $\dot{m}$ passing through the receiver in small increments to obtain a set temperature of 500 °C at the receiver outlet. Each time the mass flow is adjusted, the wall temperature and fluid property loops are repeated, until the fluid is superheated steam at 500 °C ±0.1°C.

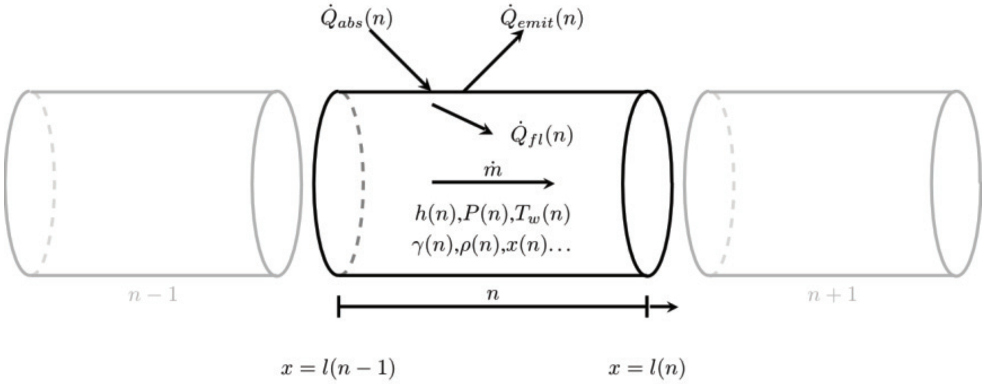

Fig. 4. Energy balance over one tube element.

All simulations were performed on a Intel Core i7-3770 CPU at 3.40GHz frequency using 7.7GiB of 1600 MHz DDR3. Evaluation of the 1,000 geometries including radiosity and ray-tracing required approximately 10 hours of processor houses on a single CPU core. Each candidate geometry detailed heat transfer simulation takes an additional 25 minutes on a single CPU core, where 90% of calculation time is spent on the detailed ray trace and the rest is spent on the energy balance.

5. Results

The results presented in this section are issued from an optimisation using parameters presented in Table 1.

Table 1. Optimisation parameters:

Maximum radius	0.75 m
Maximum depth	1.5 m
Water inlet temperature	50 °C
Steam outlet temperature	500 °C
Number of geometries g	1,000
Ray-trace scale N	$\{1, 2, 5, 10, 15, 20, 25, 30, 40, 50, 100\}.10^5$
$IC_{\mathrm{tot},s}$ array	$\{0.0282,0.0159,0.0105,0.0077,0.0061,0.0051,0.0046,0.0042,0.0036,0.0032,0.0024\}$

Fig. 5 shows the result of the radiative heat transfer stochastic optimisation method. 38 geometries passed the screening process and their performances are statistically identical in a confidence interval of $\mathrm{IC}_{\mathrm{tot},\, s_{\max}}$=0.24% corresponding to $\dot{Q}_{\mathrm{abs\ net},s_{\max}}(kW) \in [436.6, 437.5]$.

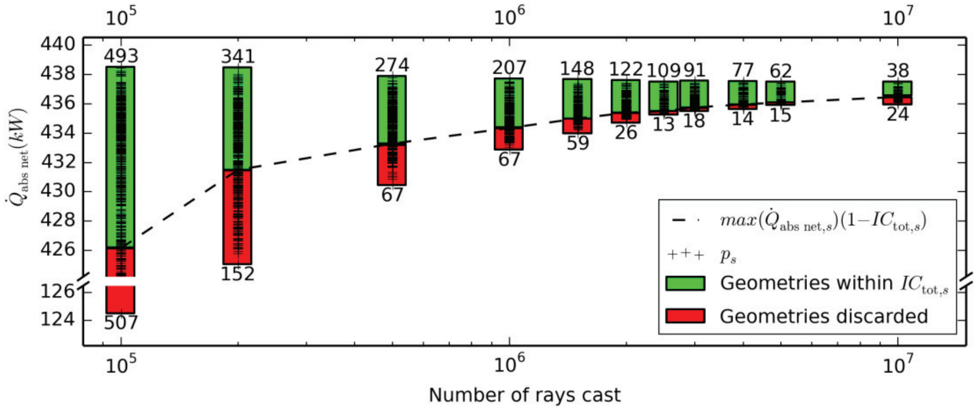

Fig. 5. Evolution of the simulated population of geometries during the stochastic optimisation process. For each $\dot{Q}_{\mathrm{abs\ net},s}$ interval, performing geometries count is shown on top and underperforming geometries count is located at the bottom of the bars.

5.1. Geometry influence on overall losses

Fig. 6 shows the efficiency η of the system for each of the 38 candidate geometries after stage 1 only and after the full 2 stages of optimisation. The efficiency is defined as the overall system efficiency: $\eta = \dot{Q}_{\mathrm{fl}}/\dot{Q}_{\mathrm{sun}}$. The improvement in the quality of the results from the detailed heat transfer model appears clearly with all geometries dropping significantly. Geometries with very similar performances from stage 1 can be differentiated and consequently ranked.

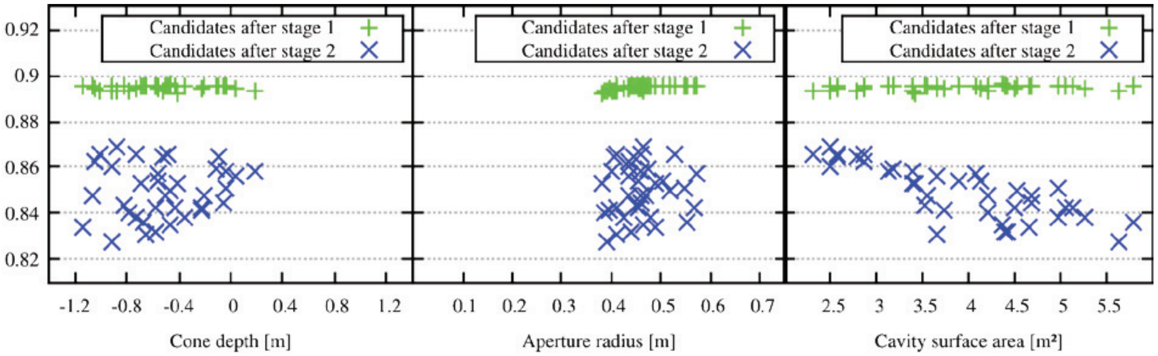

Fig. 6. System efficiency η for the 38 final candidate geometries as a function of cone depth (left), aperture radius (middle), and overall receiver wall area (right).

Cone depth values span over a large interval, suggesting that radiative losses do not impose strict constraints on the geometry of the bottom of the cavity. Aperture values are constrained in a small interval denoting the trade-off between spillage capture and thermal emission loss. Overall receiver area is relatively correlated to the efficiency of the system as suggested by Fig. 6 (right). As a general rule, the smaller the area of the receiver the higher the efficiency. The detailed heat transfer model captures more precisely the variations in efficiencies between the 38 candidates and offers a way to rank them more efficiently.

5.2. Boiling profile analysis

In Fig. 7, three geometries belonging to the 38 best candidates are presented. Case 03 is the best candidate among them, case 13 the worse and case 29 an intermediate geometry with different geometrical features.

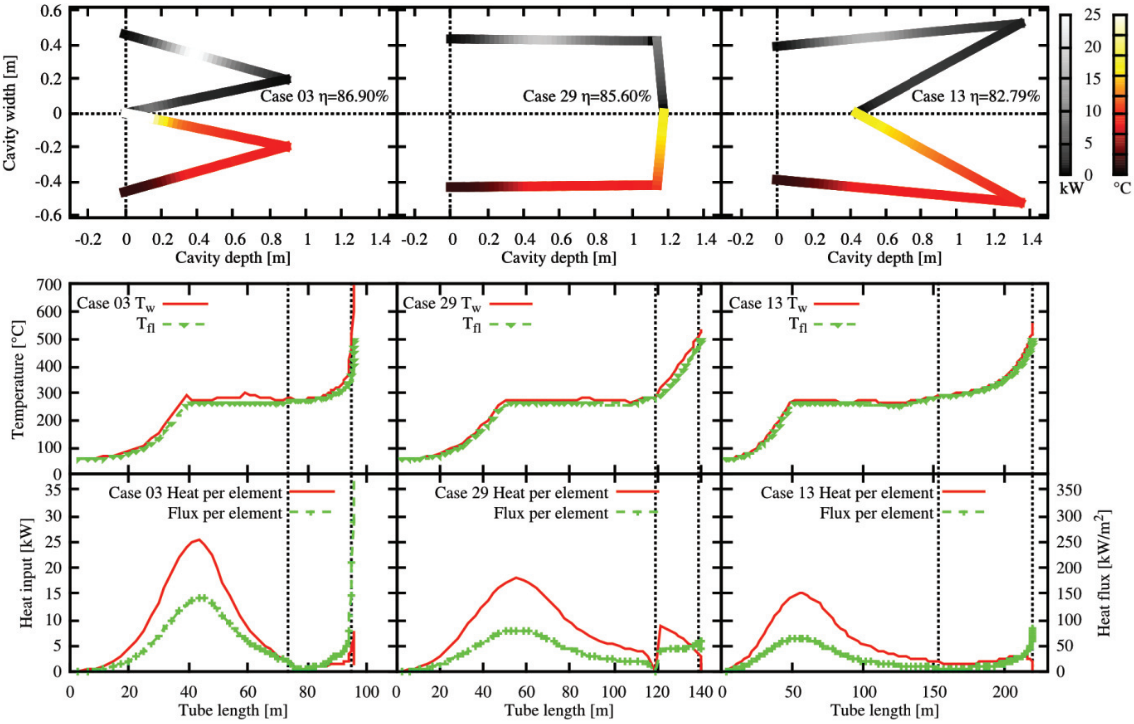

Fig. 7. Three geometries obtained after the two stages optimisation. Vertical dotted lines indicate the beginning and end of the cone element.

As show on Fig. 7, the geometrical shape of these candidates has an influence on the flux and wall temperature distributions, leading to unique boiling profiles. This is valuable information when considering receiver design. For example, case 03 is the most efficient but it exhibits very high wall temperatures near the cone center, which may impose a severe thermal stress on the absorber tube. Additionally, this hot spot seems rather close to the aperture and potentially a source of emissions. However, refined boiling profile calculations show that this effect is mitigated by the small surface area where this hot spot lies. In this case, the geometry in case 29 may be preferred, due to moderate wall temperature profiles and other practical considerations. These temperature profiles also provide the means to incorporate convective heat losses in future simulations.

6. Conclusion

A two-stage receiver geometry shape optimisation method was used to maximise the conversion of concentrated solar radiation to thermal energy carried by a water/steam flow. The method sequentially optimises expected radiative losses using a stochastic algorithm able to mitigate ray-tracing computational effort to then perform refined energy balances. The basic version of the model presented in this study is able to identify the best candidates from a net-absorbed-power point of view, and differentiate them using a detailed heat transfer model able to give information about wall temperature and radiative flux distributions in the receiver. This information is important when considering receiver design. In an upcoming study, the present methodology is applied to a different class of cavity receiver geometry defined by more geometrical parameters and additional constraints are added to the optimisation method such as tube bending radius limitations and passive surfaces.

Aknowledgements

Funding for this work was provided by the Australian Renewable Energy Agency.

References

[1] Y. Shuai, X.-L. Xia, and H.-P. Tan, “Radiation performance of dish solar concentrator/cavity receiver systems,” *Solar Energy*, vol. 82, no. 1, pp. 13 – 21, 2008. [Online]. Available: http://www.sciencedirect.com/science/article/pii/S0038092X07001235

[2] C.-A. Asselineau, E. Abbassi, and J. Pye, “Open cavity receiver geometry influence on radiative losses,” in *Proceedings of Solar2014, 52nd Annual Conference of the Australian Solar Energy Society*, Solar2014, Ed. Melbourne, May 2014.

[3] F.-Q. Wang, R.-Y. Lin, B. Liu, H.-P. Tan, and Y. Shuai, “Optical efficiency analysis of cylindrical cavity receiver with bottom surface convex,” *Solar Energy*, vol. 90, no. 0, pp. 195 – 204, 2013. [Online]. Available: http://www.sciencedirect.com/science/article/pii/-S0038092X13000339

[4] Q.-J. Mao, Y. Shuai, and Y. Yuan, “Study on radiation flux of the receiver with a parabolic solar concentrator system,” *Energy Conversion and Management*, vol. 84, no. 0, pp. 1 – 6, 2014. [Online]. Available: http://www.sciencedirect.com/science/article/pii/S0196890414002945

[5] K. Lovegrove, G. Burgess, and J. Pye, “A new 500m^2 paraboloidal dish solar concentrator,” *Solar Energy*, vol. 85, no. 4, pp. 620 – 626, 2011, solarPACES 2009. [Online]. Available: http://www.sciencedirect.com/science/article/pii/S0038092X10000228

[6] C. K. Ho, A. R. Mahoney, A. Ambrosini, M. Bencomo, A. Hall, and T. N. Lambert, “Characterization of Pyromark 2500 paint for high-temperature solar receivers,” *Journal of Solar Energy Engineering*, vol. 136, no. 1, pp. 014502–014502, Jul. 2013. [Online]. Available: http://dx.doi.org/10.1115/1.4024031

[7] D. Buie, A. Monger, and C. Dey, “Sunshape distributions for terrestrial solar simulations,” *Solar Energy*, vol. 74, no. 2, pp. 113 – 122, 2003. [Online]. Available: http://www.sciencedirect.com/science/article/pii/S0038092X03001257

[8] C. A. Gueymard, “Spectral circumsolar radiation contribution to CPV,” *AIP Conference Proceedings*, vol. 1277, no. 1, pp. 316–319, 2010. [Online]. Available: http://scitation.aip.org/content/aip/proceeding/aipcp/10.1063/1.3509220

[9] M. F. Modest, *Radiative Heat Transfer*, Elsevier, Ed. Academic Press, 2003.

[10] J. Delatorre, G. Baud, J. Bézian, S. Blanco, C. Caliot, J. Cornet, C. Coustet, J. Dauchet, M. E. Hafi, V. Eymet, R. Fournier, J. Gautrais, O. Gourmel, D. Joseph, N. Meilhac, A. Pajot, M. Paulin, P. Perez, B. Piaud, M. Roger, J. Rolland, F. Veynandt, and S. Weitz, “Monte carlo advances and concentrated solar applications,” *Solar Energy*, vol. 103, no. 0, pp. 653 – 681, 2014. [Online]. Available: http://-www.sciencedirect.com/science/article/pii/S0038092X13001448

[11] Y. Meller. Tracer package: an open source, object oriented, ray-tracing library in python language. https://github.com/yosefm/tracer. [Online]. Available: https://github.com/yosefm/tracer

[12] J. Pye, “Freesteam table properties,” simple placeholder for Freesteam reference.

[13] V. Gnielinski, “New equations for heat and mass transfer in turbulent pipe and channel flow,” *Int. Chem. Eng*, vol. 16, no. 2, pp. 359–368, 1976.

[14] B. Petukhov and V. Popov, “Theoretical calculation of heat exchange and frictional resistance in turbulent flow in tubes of an incompressible fluid with variable physical properties,” *High Temperature*, vol. 1, pp. 69–83, 1963.

[15] D. Groeneveld, “Post-dryout heat transfer at reactor operating conditions,” Atomic Energy of Canada Ltd., Chalk River, Ontario. Chalk River Nuclear Labs., Tech. Rep., 1973.

[16] S. G. Kandlikar, “Development of a flow boiling map for subcooled and saturated flow boiling for different fluids inside circular tunnels,” *Journal of Heat Transfer*, vol. 113, pp. 191–200, February 1991.